Monitoring plasmonic hot-carrier chemical reactions at the single particle level

Sabrina Simoncelli,*[a,b] Evangelina L. Pensa,[a] Thomas Brick,[a] Julian Gargiulo,[a] Alberto Lauri,[a] Javier Cambiasso,[a] Yi Li,[a,c] Stefan A. Maier[a,c] and Emiliano Cortés*[a,c]

a) The Blackett Laboratory, Department of Physics, Imperial College London, London SW7 2AZ, United Kingdom
b) Department of Physics and Randall Division of Cell and Molecular Biophysics, King's College London, London SE1 1UL, United Kingdom.
c) Chair in Hybrid Nanosystems, Nanoinstitute Munich, Faculty of Physics, Ludwig-Maximilians-Universität München, 80799 München, Germany

* E-mail: s.simoncelli@imperial.ac.uk, Emiliano.Cortes@lmu.de

ABSTRACT

Plasmon excitation in metal nanoparticles triggers the generation of highly energetic charge carriers that - properly manipulated and exploited - can mediate chemical reactions. Single-particle techniques are key to unearth the underlying mechanisms of hot-carrier generation, transport and injection as well as to disentangle the role of the temperature increase and the enhanced near-field at the nanoparticle-molecule interface. Gaining a nanoscopic insight of these processes and their interplay could aid in the rational design of plasmonic photocatalysts. Here, we present three different approaches to monitor hot-carrier reactivity at the single-particle level. We use a combination of dark-field microscopy and photo-electrochemistry to track a hot-hole driven reaction on a single Au nanoparticle. We image hot-electron reactivity with sub-particle spatial resolution using nanoscopy techniques. Finally, we push the limits looking for a hot-electron induced chemical reaction that generates a fluorescent product, which should enable imaging of active plasmonic photocatalysis at the single-particle and single-molecule levels.

INTRODUCTION

Recent years have seen tremendous progress in the design of plasmonic antennas that can amplify and confine optical fields at the nanoscale.[1] These optical antennas, fabricated with metallic nanostructures, convert free-space light into localized fields by coupling electronic-optical oscillations at the metal interface. The magnitude and spatial distribution of these high-field regions are very sensitive to the size, geometry and material of the nanostructure.[2] Indeed, these characteristics make them powerful tools to control external radiation down to the sub-wavelength regime, which, during the past two decades, have been exploited to modify the optical properties of nearby emitters, revolutionizing fields as diverse as bio-sensing and homeland security.

Besides the opportunities offered by these optical antennas to control the photophysical process of molecules, recent developments have also emerged from the combination of plasmonics and chemistry.[3] The optical excitation of surface plasmons in metallic nanostructures leads not only to strongly enhanced light scattering, but also to enhanced light absorption. The non-radiative relaxation of the plasmon, which results in the generation of energetic charge-carriers (electron–hole pairs), can serve as an efficient source of energy to trigger chemical reactions.[4, 5] Unlike semiconductors, where the properties of the carriers are determined by the band gap, plasmonic nanostructures allow versatile manipulation. The tunability of nanostructure shape, size, material and interface offers a high degree of control to tailor the energy, spatial distribution and lifetime of the plasmon-derived hot-carriers. Fine control over these processes could assist in adapting the reactivity of plasmonic nanoparticles (NPs), providing exciting opportunities for photocatalysis.[5] In this way, some of the pioneering works demonstrated the possibility of plasmonically inducing the water splitting reaction,[6] H_2 dissociation on AuNPs[7] or ethylene epoxidation and CO and NH_3 oxidation on AgNPs[8], among many others.[9-12]

Despite of the growing interest and the advances in the design of plasmonic nano-antennas that can be exploited to activate chemical transformations, there are yet many challenges regarding their use as efficient hot-carrier injectors. The overall power conversion ultimately depends on the efficient extraction of the hot-carriers before thermalization and the subsequent regeneration of the surface charge density, either by restoring loss of electrons or holes.[12, 13] In order to design efficient extraction schemes, much remains to be learnt about the energy and momentum distribution of the generated hot-carriers, the complex energy-transfer processes and the crucial role of the interface.[14-16] Furthermore, it is essential to disentangle the role of hot carriers from other phenomena

linked to plasmon-excitation and decay that can also contribute to chemical transformations, such as temperature increase and near-field enhancement.[17, 18]

Insights on the mechanistic details of hot-carriers reactivity have been recently unearth by combining optical information of the plasmonic nanomaterials with ensemble kinetic analysis of the chemical transformations, either in gas or condense-phase.[19-21] While these ensemble schemes are a powerful source to start uncovering the complex interplay of processes controlling hot-carrier reactivity, they fail to address the role of structural inhomogeneities of nanomaterials on their overall efficiency.[22] Gaining nanoscopic insight at the single particle level and *in operando* conditions is critical to guide the efficient design and fabrication of reactive plasmonic platforms, *i.e.* deciding the best shape, size, energy input, crystalline structure, reactive sites, configuration of materials (for multi-metallic ones or particle-substrate combinations), among many others.[23-26] However, pushing the current bulk-inspired methods down to the single-particle level holds the challenge of tracking chemical transformations of only few thousands of molecules.[23, 27, 28]

Here we present three different approaches to track and quantify hot-carriers reactivity on single plasmonic nanoantennas. First, we explore a plasmonic hot-hole driven reaction under *in operando* conditions using a combination of dark-field microscopy and photo-electrochemistry. Second, we show that single-molecule based super-resolution schemes can be used to map hot-carrier reactivity beyond the diffraction limit of light, which we tested by visualizing the hot-electron driven desorption of thiol anchor groups from the surface of single Au nanostructures. Finally, we demonstrate the hot-electron driven reduction of Resazurin into Resorufin using Ag Nps. This fluorogenic reaction can open up new paths to reveal nanoscopic aspects of hot-carrier driven reactions at the single-particle and single-molecule levels.

RESULTS

Hot-hole reactivity at the single particle level

We combined electrochemistry and dark-field microscopy to study the role of a photoexcited AuNP in charge transfer processes, as schematized in Figure 1a. Electrochemical control was performed using a potentiostat and a three-electrodes cell configuration. Saturated calomel electrode (SCE) and Pt coil served as reference electrode (RE) and counter electrode (CE), respectively. The working electrode (WE) consists of 80 nm AuNPs drop-casted on ITO. The electrochemical cell, with the three electrodes and filled

with the supporting electrolyte (0.5 M H_2SO_4), was mounted on a dark-field microscope with a water immersion objective. This opto-electrochemical setup allowed tuning the WE electron's energy as well as the illumination and spectroscopic characterization of single nanoparticles.[29]

As a first example of the capabilities of our setup, we monitored the changes in the optical properties of a single AuNP when the electro-oxidation and electro-reduction of its capping layer takes place. As shown in Figure 1b-i, the WE consists of AuNPs capped with polyaniline (PANI) and drop-casted on a ITO substrate. Figure 1b-ii shows that the PANI redox state can be switched by the applied potential, as depicted by the cyclic voltammogram curve of the system and the inset scheme of the reaction. As the potential (E) increases linearly from -0.05 to 0.45 V, the AuNPs drains electrons from the PANI layer, oxidizing it. As a result of the charge transfer process the current increases, peaking at 0.2 V. Note that the final state (at 0.4 V) possess a higher current value than the initial one (at -0.05 V), characteristic of a more conductive PANI layer.[30] When reversing the scan from 0.4 V to -0.05 V, the AuNPs inject electrons into the PANI layer and a reduction peak is observed at 0.1 V. It must be noted that the measured current is an ensemble property corresponding to the total number of AuNPs (acting as WE) on the ITO substrate. In order to monitor the process at the single-particle level we turned to follow the optical changes (*i.e.* the scattering spectra) of a single AuNP while applying the electrochemical scan.

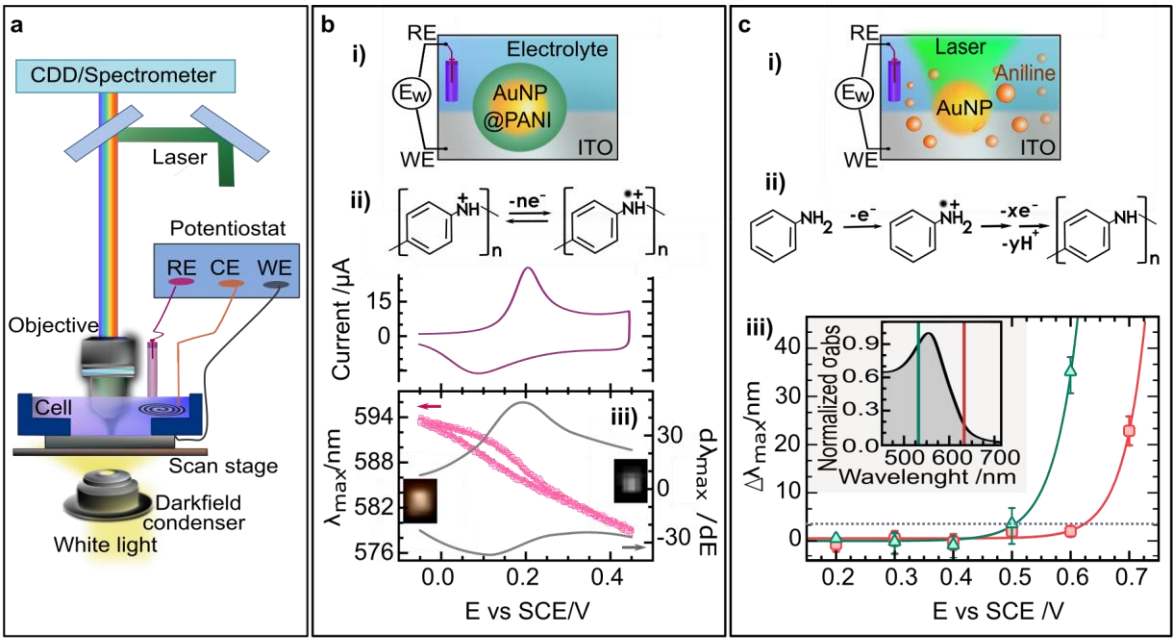

Figure 1. Opto-electrochemical measurements of single AuNPs. (a) Scheme of the optoelectrochemical setup. (b) Monitoring the oxidation/reduction of the AuNP capping layer (polyaniline, PANI) at the single-particle level. (i) Composition of the WE: PANI capped AuNPs (AuNPs@PANI) on ITO. (ii) Cyclic voltammogram of PANI on pollycrystalline Au. The upper inset depicts the redox reaction. (iii) Maxima scattering wavelength (λ_{max}) of a single AuNP@PANI as a function of E (pink dots). Inset: dark-field images of a single AuNP@PANI at the two limit potentials. By derivation of the spectroelectrochemical data it is possible to recorver the redox profiles for PANI oxidation and reduction at the single particle level (grey solid lines). In all cases the applied potential was set between -0.05 to 0.45 V (vs SCE) at 0.05 V s^{-1}. (c) Plasmon-assited electropolymerization of aniline. (i) Scheme of the WE: AuNPs drop-casted on ITO. The reaction is conducted in aniline solution and under CW laser illumitation. (ii) Simplified aniline polymerization mechanism highlighting that radical formation is the limiting rate step. (iii) Red-shift in the maxima scattering wavelength ($\Delta\lambda_{max}$) after AuNPs were illuminated for 30 s at the given potential E with either 532 nm (green dots) or 633 nm (red squares) CW lasers. The irradiance for each laser wavelenght was choosen such that the absorbed power by AuNP is the same.

It has been shown that PANI dielectric function drastically changes depending on its redox state, being lower for the oxidised state.[31] Therefore, the optical properties of AuNPs coated with PANI are expected to change when performing a cyclic voltammetry scan similar to the one described in Figure 1b-ii.[32] Following the approach developed by the Landes group,[33] we performed a single-particle electrochemical experiment but, in this case, we monitored the redox changes in the PANI capping layer through the optical response of a single AuNP. We used dark-field microscopy to localize and track changes at the single particle level. Dark-field scattering spectra of a single PANI-capped AuNP (PANI@AuNP) were recorded as the potential was cyclically scanned between -0.05 and 0.45 V. Figure 1b-iii shows that the AuNP scattering peak (λ_{max}) blue-shifts when the potential is increased and red-shifts when the potential is decreased (see pink curve). The non-linear response and the hysteresis observed in λ_{max} vs E - when comparing the direct and the reverse electrochemical scans - reveals a non-reversible redox behaviour for the PANI layer of this AuNP (*i.e.* the PANI oxidation and reduction peaks are centered at different potentials). This can be further extracted when performing the derivative of the scattering peak against the applied potential ($d\lambda_{max}/dE$), as shown in the grey curves of Figure 1b-iii. In this way, it is possible to recover the electrochemical response of a single AuNP from the optical changes in its scattering spectra.[33] This is further reinforced by the similarity between the electrochemically-measured cyclic voltammogram for many AuNPs (Figure 1b-ii) and the optically-extracted redox behaviour of a single AuNP (Figure 1b-iii).

Taking avantage of the single-particle sensitivity and the precise electrochemical control of the WE electron's energy, we finally studied the electro-oxidation of aniline on an optically excited AuNP. This configuration could assist in revealing the quanta of energy supplied by the illuminated AuNP in order to drive the oxidation process: we should be able to monitor changes in the potential required to drive the reaction if there is any photocatalytic contribution from the AuNP. To this end, AuNPs were drop-casted on ITO and immersed in an aniline solution (Fig. 1c-i). The potential was step-incresed by 0.1 V from 0.2 to 0.7 V - as an oxidation needs to take place - as shown in the diagram of Figure 1c-ii.

For each applied potential, the AuNP was excited for 30 seconds of illumination with a diffraction-limited CW laser coupled throught a water immersion objective (see Fig 1a). Two laser lines were employed: 532 nm and 633 nm. This allowed us to explore two nearly extreme situations: maximium and minimum of the absorption spectra for the 80 nm AuNP (see inset in Figure c-iii). Laser irradiance were set at 2.2 mW/cm^2 and 9.3 mW/cm^2 for 532 nm and 633 nm, respectively. These values guarantee that the absorbed power - and therefore the increse in temperature - is the same for both wavelenghts. Figure 1c-iii shows the shift in the scattering peak ($\Delta\lambda max$) as a function of the applied potential after single AuNPs were subjected to laser illumination. Green dots corresponds to a AuNP iluminated at 532 nm while the red squares corresponds to 633 nm illumination. In both cases, after a certain potential, a drastic red-shift in the scattering peak is observed. These changes in the scattering spectra are due to PANI formation around the AuNP. Interestingly, the aniline polymerization starts at different potentials for both irradiation wavelenghts. For 532, a red-shift of $\Delta\lambda_{max} = 3.4$ nm is observed at 0.50 V, while for 633nm the same red-shift is reached at 0.62 V (see dotted line in Fig c-iii). This result is even more surprising when considering that the absorbed power is the same for both wavelengths and thus the increase in temperature is the same. Being aniline a transparent molecule in the visible regime also rules out any possible near-field contribution or excitation.[18] Hence, these results suggest that the electrochemcial reaction is plasmon-catalyzed by the generated hot-holes on the AuNP and that the energy of the available holes depends on the excitation wavelenght of light.

These results show that photo-electrochemical measurements can serve as a route to estimate the energy and efficiency of plasmon generated hot-carriers in single particles, revelling unknown aspects of the light-induced electron transfer mechanism. We then turned to explore the spatial reactivity of single plasmonic photocatalysts.

Hot-electron reactivity-mapping at the single-particle level

During the last years, single-molecule based super-resolution fluorescence microscopy techniques have emerged as a versatile method to map molecular targets with nanometer precision (*i.e.* beyond Abbe's diffraction limit of light).[34] By separating the fluorescence emission of individual fluorophores in time using photo-conversion, photo-switching or transient binding approaches, these techniques can provide high resolution information thanks to the subsequent determination of the single fluorophore's position.[35] Borrowing these ideas, we developed a nanoscopic approach that enables imaging of reactive sites in plasmonic photocatalysts.

Figure 2a illustrates the concept of our imaging approach, named metallic DNA-PAINT (m-PAINT).[36, 37] DNA-PAINT (DNA points accumulation for imaging in nanoscale topography),[38] is a recently developed localization based super-resolution nanoscopy technique that uses single-stranded fluorescently-label DNA probes (imager strands) which transiently bind and quickly dissociate from their complementary DNA targets (docking strands) to reconstruct super-resolved images. In m-PAINT, we combined this technique with single-particle femtosecond illumination to map the plasmon-induced hot-electron active sites on the surface of metallic nanomaterials.[36, 37]

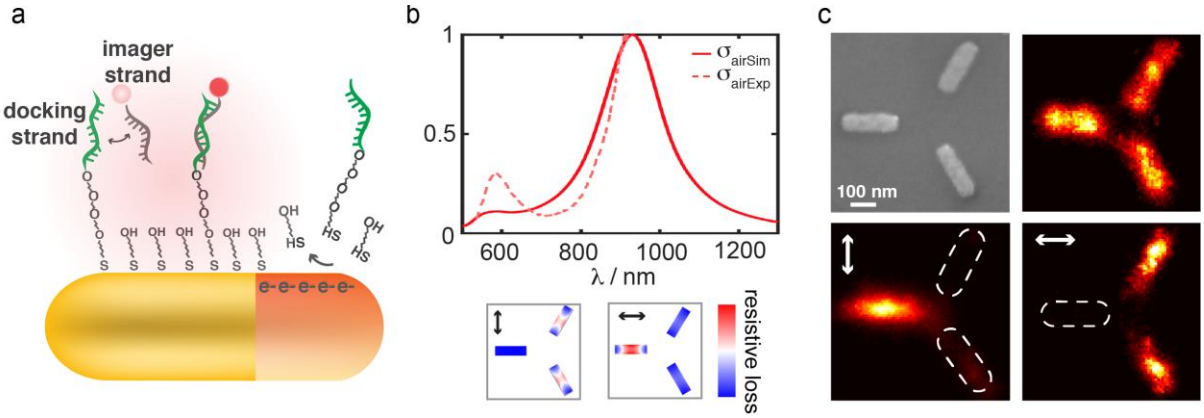

Figure 2. Chemical-desorption mapping of thiolated-DNA molecules upon plasmonic hot-electron transfer. (a) Schematic of metallic DNA-PAINT. Docking strands (thiolated-DNA) are immobilized onto the Au surface of the plasmonic element providing transient binding sites for the complementary fluorescently-label DNA strands (imager strands). Upon plasmon excitation and hot-electron transfer, some docking strands are desorbed from the surface. (b) Optical performance of the Au trimer nanorods antenna. Each nanorod has a dimension of 180×55 nm^2. Top: Calculated (solid line) and experimental (dashed line) scattering cross-section. Bottom: Near-field maps

of absorbed power in water (or resistive loss maps) for vertical or horizontal polarizations at 950 nm excitation. (c) Scanning electron microscope image of the plasmonic structure. Super-resolution m-PAINT images for the non-irradiated sample and for the vertical/horizontal polarization excitation with 220 fs laser illumination at 950 nm wavelength. Dashed curves indicate the borderline of the Au elements where the thiol-desorption has taken place (*i.e.* there is no-binding of the imager strand).

First, we chemically coupled DNA targets (docking strands) to the surface of metallic nanostructures through a binder ligand. Mindful design of the binder ligand is of paramount importance to both: (i) achieve highly-resolved images and (ii) study different hot-electron reactions (*i.e.* by changing the functional anchor group of the binder or by incorporating an electron-acceptor molecule in it). To optimize the imaging capabilities of our technique, we set the docking strand height between the fluorophores and the metallic surface to ∼ 7 nm, which diminishes the spatial fluorescence quenching effects on metals.[39] In our case, this was achieved by introducing a hydrophilic PEG unit in the form of hexaethylene glycol between the docking strand and a mercaptohexyl linker. Additionally, we use a backfilling molecule (6-mercapto-1-hexanol, MCH) to ensure a more compact monolayer and therefore prevent unspecific binding of DNA strands on the surface of the metallic nanostructure.[40] Our experimental approach allowed the imaging of single Au trimer nanorods structures with nanometric resolution (Figure 2c, top right) - perfectly agreeing with the scanning electron microscope (SEM) images (Figure 2c, top left).

Then, we studied the hot-electron driven cleavage of Au-sulfur bonds using an Au trimer nanorod system. Figure 2b (top) shows the scattering spectrum of the system in air. A plasmonic dipolar resonance is present at 910 nm, corresponding to the resonance of each individual rod. At this wavelength, the scattering spectra of the system is independent of the excitation polarization (data not-shown). However, the spatial distribution of the non-radiative decay that govern the generation of hot electrons can largely differ between sub-elements depending on light polarization.[36] Figure 2b (bottom) depicts the near-field power absorption maps (also named as resistive loss maps in the literature) for the two polarizations. We illuminated the system using a linearly polarized 950 nm femtosecond laser. Spinning the polarization of incident light, it is possible to selectively excite either the horizontal rod or the two diagonal rods. Figure 2c (bottom) shows m-PAINT images of the trimers after irradiation. Dark areas of the antennas indicate the places where photocleavage has occurred while bright areas indicate remaining binding domains after irradiation. Resemblance between m-PAINT maps and simulated absorption maps for both polarizations proves that the spatial distribution

of energetic electrons responsible to trigger the Au-S bond cleavage can be imaged with sub-diffraction resolution.

Hot-electron reaction for tracking in operando single-photocatalyst activity

This section aims at pushing the study of hot-carrier reactions from the single photocatalyst to the single molecule level as they happen *in situ*. Single-molecule studies of single nanocatalysts have been recently implemented using fluorogenic reactions,[28, 40] where a non-fluorescent reactant is converted into a fluorescent product. One of the most employed of such reactions is the reduction of the non-fluorescent Resazurin (Rz) molecule when reacting with hydroxylamine on the surface of Au nanoparticles (heterogeneous catalysis) to produce the highly fluorescent Resorufin (Rs) molecule,[28] as schematized in Figure 3a. The high sensitivity of fluorescence allows the detection and quantification of single turn-over events, which appears as a spike in the collected fluorescence signal, as shown in the inset of Figure 3a. Following this approach, kinetics studies of several single heterogeneous nanocatalysts were studied revealing reaction pathways,[28] size[40] and facet dependence,[41] sub-particle distribution of active sites[34] or even activation energies.[42]

In order to extend this technique to the study of hot-carrier driven chemical reactions at the single photocatalyst and single molecule levels it is crucial to find a fluorogenic reaction driven by hot-carriers. Here, we show that Ag spherical nanoparticles (AgNPs) illuminated at their plasmon resonance can produce hot-electrons capable of reducing Rz into Rs without using hydroxylamine or any other reducing agent, as schematized in Figure 3b.

We carried out ensemble-level fluorescence measurements to study the photocatalysis of Rz to Rs in the presence of plasmonic 60 nm AgNPs. Figure 3c shows the absorption spectra of these three components. Due to excitation of the plasmon resonance, the AgNPs present an absorption maximum at 430 nm. We illuminated a cuvette containing 20 pM of AgNPs and 5 μM Rs with a 405 nm CW laser at a power density of 300 mW/cm^2. At this wavelength, direct absorption of light by Rs or Rz is very low. Figure 3d illustrates the fluorescence spectra variation for increasing irradiation times. Before irradiation, (red curve) an emission peak of weakly fluorescent Rz at 634 nm can be observed. In addition, a small number a highly fluorescent Rs molecules contribute to an emission peak at 585 nm. Dye conversion can be followed through the increase and accompanying decrease in the fluorescence emission peaks of Rs and Rz, respectively. After 150 minutes, almost the entire solution is converted, with the

final spectra resembling the Rs one. Pertinent controls performed in the absence of AgNPs or without illumination showed no significant conversion. These experiments effectively demonstrate that it is possible to photocatalyse the reduction of Rs into Rz when exciting the plasmon resonance of the AgNPs. However, plasmonic NPs can catalyse chemical transformations due to enhanced fields, thermal effects, or by the generated carriers.[5] In order to prove that this reaction can be used as a hot-electron probe, thermal and field induced conversion should be ruled out.

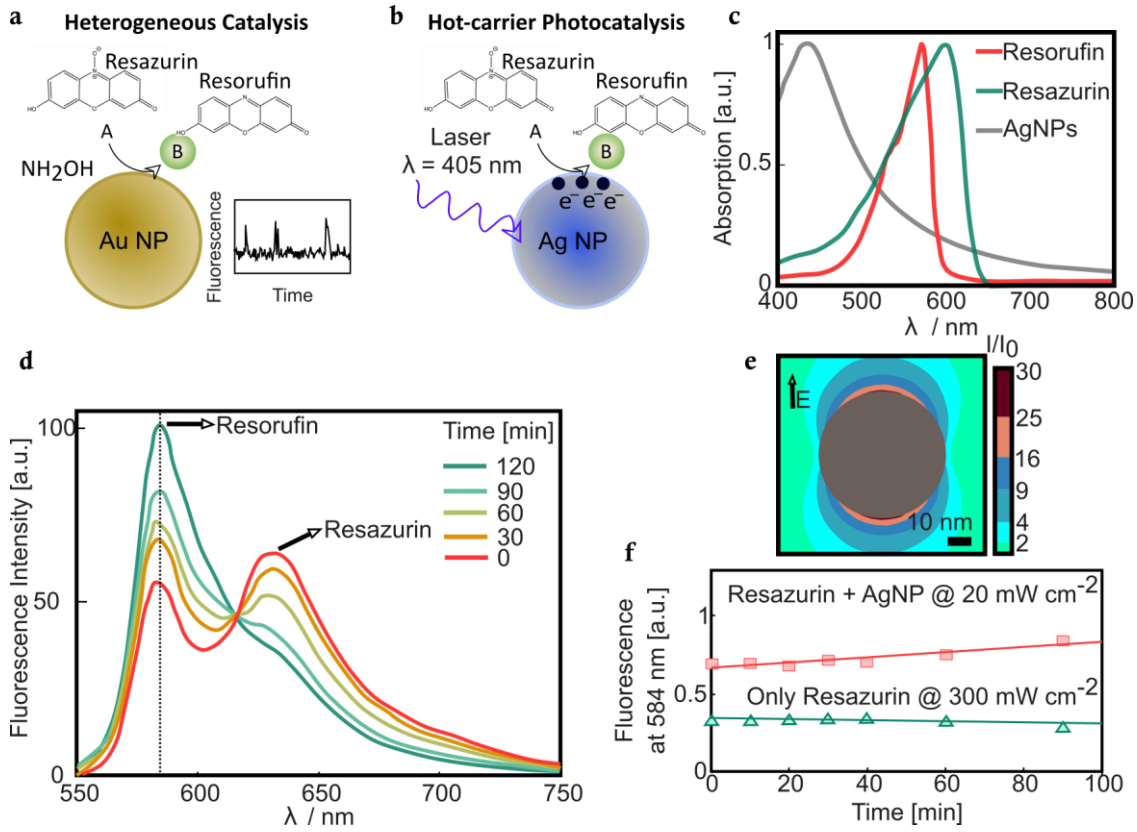

Figure 3. (a) Example of a Heterogeneous Catalysis experiment. A non-fluorescent molecule **A** is converted into a highly fluorescent one **B** on the nanocatalyst surface. Each turn-over event is detected as a spike in the fluorescence signal. (b) Working principle of the Hot-carrier driven photocatalysis. A plasmonic Ag NP is resonantly illuminated with a continuous wave laser at 405 nm, generating highly energetic electrons. These electrons reduce the non-fluorescent Resazurin into the fluorescent Resorufin. (c) Normalized absorption spectra of 60 nm Ag nanoparticles (grey), Resorufin (red) and Resazurin (green). (d) Photoconversion of an initial 5 μM Resorufin solution (red) for increasing irradiation times. Spectra was normalized to the iso-emissive point at 613 nm. Vertical dashed line indicates Rs emission peak at 584 nm used in figure 3f (e) Map of the intensity enhancement produced by a 60 nm Ag sphere illuminated at 405 nm. Polarization of the beam is indicated with an arrow. (f) Fluorescence intensity at the Resazurin peak (584 nm) vs. time for a solution containing 5 μM

Resazurin and 20 pM Ag NPs illuminated at 20 mW cm^{-2} (pink) and for a solution of 5 μM Resazurin without Ag NPs and 15 times more power 300 mW cm^{-2} (green). Curves have been vertically shifted for comparison.

The temperature increase ΔT of an illuminated single AgNP can be estimated using $\Delta T = \frac{\sigma_{abs} I}{4\pi k a}$, with σ_{abs} the absorption cross section, I the irradiance, k the thermal conductivity of the immersion media and a the NP radius.[43] Applying this function using σ_{abs}= 1.2 10^{-14} m^2, k = 0.59 W K/m and a = 30 nm we envisage a negligible temperature increase on the order of just $10^{-4}K$. The above assumes an isolated nanoparticle, but recent studies showed that collective effects for highly concentrated solutions can lead to a marked temperature rise of the solution, some orders of magnitude greater than the one expected for isolated NPs.[44] In order to rule out such macroscopic temperature rises a thermocouple probe was inserted into a solution of 20 pM Ag nanoparticles and the solution was illuminated with a 405 nm laser at the maximum power intensity used in our experiments. No temperature increase was measured, meaning that the temperature increase is smaller than the sensitivity of the thermocouple (0.1 K).

Then, we investigated if the conversion reaction can be attributed solely to the enhancement in electric field around the NPs upon resonant illumination. Figure 3e depicts Finite difference time domain (FDTD) calculations of field intensity enhancements around a 60 nm diameter Ag NP suspended in water upon illumination at 405 nm. Within a shell of 10 nm around the nanoparticle surface, the average field intensity over all three planes is 14.9 times greater than that of incident wave. We can then rule out the notion that it is solely a field induced effect through a comparison of the dye conversion with and without nanoparticles, using 15 times higher power density in the latter case (see Figure 3f). This way, both systems exhibit the same magnitude of field intensity. Figure 3d shows the fluorescence intensity at the emission peak of Rs as a function of time. When in the absence of Ag and using 15 times higher beam intensity (300 mW/cm^2), no clear increase in the peak fluorescence values is observed. For lower beam intensities (20 mW/cm^2) in the presence of Ag NPs, a slight but discernible increase in the peak intensity over time is observed, indicative of the conversion of Rz to Rs. The lower magnitude of this conversion relative to that illustrated in Figure 3d is to be expected given the low laser power involved.

The results presented here allow us to claim that the reduction of Rz to Rs is driven by hot-carriers induced upon resonant excitation of plasmons in Ag nanoparticles. This result paves the way for the investigation of hot-carriers reaction at the single molecule level.

CONCLUSIONS

Rational design of plasmonic photocatalysts requires deeper understanding of the mechanisms contributing to plasmon-induced chemical reactions. Single-particle and single-molecule studies are aimed to decouple ensemble effects, facilitating the interpretation of the experimental results and offering easier paths to improve the performance of the photocatalyst under *in operando* conditions. This has been exemplified in the present contribution through the study of the energy or spatial distribution of plasmonic hot-carriers in single plasmonic particles coupled to different reactive interfaces. Finally, we have shown the reaction conditions in order to drive a hot-electron conversion of a fluorogenic molecule, which could serve as a reactive probe for future single-molecule studies under a diverse number of super-resolution schemes.

EXPERIMENTAL

Sample preparation for opto-electrochemical measurements.

All reagents are high-purity and were used as received. For aqueous solutions, ultra-pure water was employed (18.2 MΩ·cm, MilliQ®). AuNPs (80 nm in diameter, capped with CTAB, OD solution: 0.05) were synthetized and purified according to Yoon J. H. et al.[46] AuNPs@PANI were obtained by chemical synthesis of PANI layers (19 nm in thickness) around the above AuNPs following the protocol descripted by Xing S. et al.[47]

Sample preparation for hot-electron reactivity mapping.

Gold trimer nanorods with dimensions of 180×55 nm^2 were fabricated on borosilicate glass using electron beam lithography (E-line, Raith GmbH). The substrate was first coated with positive-tone poly(methyl methacrylate) (950 K A4) resist and posteriorly baked for 3 min at 180 °C. The nanostructures were then defined by an electron beam exposure, followed by a development procedure. Chromium and gold thermal evaporation at 1.5 Å/s (Amod, Angstrom Engineering Inc.) and a standard lift-off process at 70 °C completed the fabrication process. For DNA functionalization the samples were first left for 1.5 min in a UVO cleaner/oxidizer

(Femto, Diener Electronic GmbH) and mounted to a bottomless self-adhesive slide (sticky-Slide VI 0.4, Ibidi) to form a flow chamber with an inner volume of ~ 30 µL. DNA functionalization was performed by overnight incubation at RT of a 1 µM solution of the single stranded DNA docking strand (ThiolC6-SpacerC18-ATGAGTTAATT, biomers.net GmbH) diluted in 10 mM TRIS-HCl, 1M NaCl, pH = 7 (buffer A). Next, the sample was incubated with a 1 mM 6-Mercapto-1-hexanol (MCH, Sigma Aldrich) solution (30 minutes, RT) prior a high-volume wash with buffer A. Finally, the sample was left in 10 mM TRIS-HCl, 50 mM NaCl, pH = 7 (buffer B) or 5 mM TRIS-HCl, 10 mM MgCl2, 1 mM EDTA, pH = 8 (buffer C) for femtosecond pulsed laser irradiation or fluorescence imaging, respectively, after washing it with buffer B.

For scanning electron microscopy imaging, a 20 nm thin film of Espacer 300Z was coated onto the sample before DNA functionalization at 2000 rpm for 60 s, followed by a 60 s, 90 °C bake.

Dark-field microscopy and spectroscopy.

Optical measurements for the opto-electrochemical configuration were performed in a Witec microscope. For dark-field imaging, the sample was illuminated from the bottom with a white light source (OSL2, Thorlabs, United States) through an oil-immersion dark-field ultra-condenser (NA=1.2−1.4, Zeiss, Germany). Scattered light was collected with a water immersion objective (NA= 1.0, x63 magnification, Zeiss, Germany) and directed to the colour CCD camera. Scattering spectra were recorded before and after each AuNP was illuminated. Single-particle dark-field scattering spectroscopy of the gold trimer nanorods in air were measured with an upright Nikon Eclipse Ti-U microscope (Nikon Instruments) equipped with a dark-field objective (Nikon LU Plan ELWD 100× NA 0.80), which is used for both, to provide the incident illumination and to collect the scattered light. For illumination, a 100 W halogen lamp (Nikon) was used. The scattered light was measured with a diffractive grating and charge-coupled device camera cooled to 70 K. The plotted spectra are corrected for the system wavelength response (by measuring the cross section of a perfect reference white rough scatter) and also for dark and background counts.

Electrochemistry.

Electrochemical measurements were performed at room temperature (24.0 ± 0.2 ºC) in a three-electrode configuration cell and with a CHI760C potentiostat (CH Instruments, United States). 0.5 M H_2SO_4 (99.99%, Sigma-Aldrich) aqueous solution was employed as supporting

electrolyte. Aniline (99%, Sigma Aldrich) was dissolved in the supporting electrolyte until a final concentration of 0.2 M. The working electrode consists in 80 nm Au nanoparticles drop-casted on ITO (Nanoscribe, Germany). A Pt coil (99.99%, Goodfellow, UK) and saturated calomel electrode (SCE) served as counter and reference electrode, respectively. Before every experiment the Pt coil was cleaned using a butane flame annealing process followed by a quenching procedure in ultrapure water.

Femtosecond pulsed-laser irradiation.

For femtosecond pulsed-laser irradiation of individual gold trimer nanorods a pulsed Yb:KGW PHAROS laser system was used as the pump of an ORPHEUS collinear optical parametric amplifier with a LYRA wavelength extension option (Light Conversion Ltd., pulse duration of 180 fs, repetition rate of 100 kHz). The excitation beam (λ = 950 nm) was reflected by a short-pass dichroic mirror (Thorlabs DMSP805) and focused onto a ~ 1 μm^2 spot on the sample with a 40× (CFI S Plan Fluor ELWD 40×, NA 0.60, Nikon) air objective. The beam polarization was adjusted with a half-wave plate and a polarizer and the power fluence was set to 1.7 mJ/cm^2. The sample was fixed to an XYZ piezo-scanner stage (Nano-Drive, Mad City Laboratories), which allows automatic single nanoantenna irradiation (10 seconds per antenna). Alignment of the antennas with the excitation beam was possible by inspecting the sample with white light illumination and detecting the sample using a CCD camera (QICAM Fast 1394, QImaging).

Fluorescence microscopy imaging.

Fluorescence imaging was carried out in an inverted Nikon Eclipse Ti−U microscope (Nikon Instruments). The excitation beam at 640 nm was provided by a 20 mW CW laser (LDH, Picoquant) spectrally filtered with a clean-up filter (BrightLine HC 636/8, Semrock). A single-edge dichroic beam splitter (Semrock BrightLine FF 649) was used to reflect the excitation light into the 100×, 1.49 NA oil immersion Apo DIC N2 TIRF objective. Fluorescence light was spectrally filtered using an emission filter (ET705/72m, Chroma Technology) and collected onto an electron-multiplying charge-coupled device (EMCCD) camera (Evolve 512 Delta, Photometrics) operated at 100 ms per frame. For DNA-PAINT imaging a solution of the imager strand (Atto655-TTAACTCATG-3', biomers.net GmbH) diluted to the 5 nM in buffer C was flown into the sample immediately before starting the measurements. 20,000 frames per super-resolution image were recorded at an excitation intensity of 450 W/cm^2.

Super-resolution data processing and image analysis.

m-PAINT images were reconstructed from the raw data based on subsequent localization of single molecules via Gaussian fitting using the rainSTORM Matlab application. Prior single-molecule localization, stage drift correction, and background subtraction of the photoluminescence (static, autofluorescence emission) from the gold trimer nanorods were performed with an in-house Matlab routine. Images of individual gold trimer nanorods were reconstructed from ~ 700 to 3000 localizations. Particle averaging of gold trimer nanorods was performed using a translation registration algorithm (Matlab built-in function). Average m-PAINT images were usually reconstructed by overlying superresolution images of 30 to 36 individual gold nano-antennas that had been exposed to the same chemical/optical conditions.

Resarzurin photoconversion.

Absorption spectra were measured using a UV-Vis Agilent Technologies Cary 60 spectrometer. Fluorescence spectra were measured using an Agilent Technologies Cary Eclipse Spectrophotometer, exciting at 520 nm and monitoring from 530 – 800 nm.

A 10 mm optical path fused quartz cuvette was illuminated using a continuous wave Coherent Cube laser expanded through a telescope to a beam waist of 1 cm, so the entire solution was illuminated. After a determined irradiation time the cuvette was removed from the beam path and measured in the spectrometer.

Numerical simulations.

Numerical calculations of absorption and scattering cross-section spectra and the near-field intensity distributions were performed using both Lumerical FDTD 2017a and Comsol Multiphysics v4.4.[36]

ACKNOWLEDGMENTS

This work has been supported by the EPSRC through the Reactive Plasmonics Programme (EP/M013812/1), the Royal Society, and the Lee-Lucas Chair in Physics. S.S. acknowledges financial support from the Human Frontier Science Program Organization through a postdoctoral fellowship. J. G. acknowledge financial support from the European Commission through a Marie Skłodowska-Curie fellowship. Y. L. acknowledge the funding from the European Union's Framework Programme for Research and Innovation Horizon 2020 (2014-2020) under the Marie Skłodowska-Curie Grant Agreement No. 754388 and from LMU

Munich's Institutional Strategy LMU excellent within the framework of the German Excellence Initiative (No. ZUK22). E. C. acknowledge financial support from the European Commission through ERC Starting Grant CATALIGHT (802989).

REFERENCES

1. Halas, N.J., Lal, S., Chang, W.-S., Link, S. & Nordlander, P. Plasmons in Strongly Coupled Metallic Nanostructures. *Chemical Reviews* **111**, 3913-3961 (2011).
2. Giannini, V., Fernández-Domínguez, A.I., Heck, S.C. & Maier, S.A. Plasmonic Nanoantennas: Fundamentals and Their Use in Controlling the Radiative Properties of Nanoemitters. *Chemical Reviews* **111**, 3888-3912 (2011).
3. Linic, S., Christopher, P. & Ingram, D.B. Plasmonic-metal nanostructures for efficient conversion of solar to chemical energy. *Nature Materials* **10**, 911 (2011).
4. Brongersma, M.L., Halas, N.J. & Nordlander, P. Plasmon-induced hot carrier science and technology. *Nature Nanotechnology* **10**, 25 (2015).
5. Cortés, E. Efficiency and Bond Selectivity in Plasmon-Induced Photochemistry. *Advanced Optical Materials* **5**, 1700191 (2017).
6. Mubeen, S. et al. An autonomous photosynthetic device in which all charge carriers derive from surface plasmons. *Nature Nanotechnology* **8**, 247 (2013).
7. Mukherjee, S. et al. Hot Electrons Do the Impossible: Plasmon-Induced Dissociation of H2 on Au. *Nano Letters* **13**, 240-247 (2013).
8. Christopher, P., Xin, H. & Linic, S. Visible-light-enhanced catalytic oxidation reactions on plasmonic silver nanostructures. *Nature Chemistry* **3**, 467 (2011).
9. Oshikiri, T., Ueno, K. & Misawa, H. Selective Dinitrogen Conversion to Ammonia Using Water and Visible Light through Plasmon-induced Charge Separation. *Angewandte Chemie International Edition* **55**, 3942-3946 (2016).
10. Zhang, X. et al. Product selectivity in plasmonic photocatalysis for carbon dioxide hydrogenation. *Nature Communications* **8**, 14542 (2017).
11. Robatjazi, H. et al. Plasmon-induced selective carbon dioxide conversion on earth-abundant aluminum-cuprous oxide antenna-reactor nanoparticles. *Nature Communications* **8**, 27 (2017).
12. Xie, W. & Schlücker, S. Hot electron-induced reduction of small molecules on photorecycling metal surfaces. *Nature Communications* **6**, 7570 (2015).
13. Kim, Y., Dumett Torres, D. & Jain, P.K. Activation Energies of Plasmonic Catalysts. *Nano Letters* **16**, 3399-3407 (2016).
14. Tagliabue, G. et al. Quantifying the role of surface plasmon excitation and hot carrier transport in plasmonic devices. *Nature Communications* **9**, 3394 (2018).
15. Kale, M.J. & Christopher, P. Plasmons at the interface. *Science* **349**, 587-588 (2015).
16. Chavez, S., Aslam, U. & Linic, S. Design Principles for Directing Energy and Energetic Charge Flow in Multicomponent Plasmonic Nanostructures. *ACS Energy Letters* **3**, 1590-1596 (2018).
17. Kazuma, E., Jung, J., Ueba, H., Trenary, M. & Kim, Y. Real-space and real-time observation of a plasmon-induced chemical reaction of a single molecule. *Science* **360**, 521-526 (2018).
18. Violi, I.L., Gargiulo, J., von Bilderling, C., Cortés, E. & Stefani, F.D. Light-Induced Polarization-Directed Growth of Optically Printed Gold Nanoparticles. *Nano Letters* **16**, 6529-6533 (2016).
19. Boerigter, C., Campana, R., Morabito, M. & Linic, S. Evidence and implications of direct charge excitation as the dominant mechanism in plasmon-mediated photocatalysis. *Nature Communications* **7**, 10545 (2016).
20. Li, K. et al. Balancing Near-Field Enhancement, Absorption, and Scattering for Effective Antenna–Reactor Plasmonic Photocatalysis. *Nano Letters* **17**, 3710-3717 (2017).

21. Wu, K., Chen, J., McBride, J.R. & Lian, T. Efficient hot-electron transfer by a plasmon-induced interfacial charge-transfer transition. *Science* **349**, 632-635 (2015).
22. Cortés, E. et al. Plasmonic hot electron transport drives nano-localized chemistry. *Nature Communications* **8**, 14880 (2017).
23. Wu, C.-Y. et al. High-spatial-resolution mapping of catalytic reactions on single particles. *Nature* **541**, 511 (2017).
24. Zhan, C. et al. From plasmon-enhanced molecular spectroscopy to plasmon-mediated chemical reactions. *Nature Reviews Chemistry* **2**, 216-230 (2018).
25. Liu, L. & Corma, A. Metal Catalysts for Heterogeneous Catalysis: From Single Atoms to Nanoclusters and Nanoparticles. *Chemical Reviews* **118**, 4981-5079 (2018).
26. Novo, C., Funston, A.M. & Mulvaney, P. Direct observation of chemical reactions on single gold nanocrystals using surface plasmon spectroscopy. *Nature Nanotechnology* **3**, 598 (2008).
27. Sambur, J.B. & Chen, P. Approaches to Single-Nanoparticle Catalysis. *Annual Review of Physical Chemistry* **65**, 395-422 (2014).
28. Xu, W., Kong, J.S., Yeh, Y.-T.E. & Chen, P. Single-molecule nanocatalysis reveals heterogeneous reaction pathways and catalytic dynamics. *Nature Materials* **7**, 992 (2008).
29. Wang, W. Imaging the chemical activity of single nanoparticles with optical microscopy. *Chemical Society Reviews* **47**, 2485-2508 (2018).
30. Nicolas-Debarnot, D. & Poncin-Epaillard, F. Polyaniline as a new sensitive layer for gas sensors. *Analytica Chimica Acta* **475**, 1-15 (2003).
31. Leroux, Y. et al. Tunable Electrochemical Switch of the Optical Properties of Metallic Nanoparticles. *ACS Nano* **2**, 728-732 (2008).
32. Ding, T., Mertens, J., Lombardi, A., Scherman, O.A. & Baumberg, J.J. Light-Directed Tuning of Plasmon Resonances via Plasmon-Induced Polymerization Using Hot Electrons. *ACS Photonics* **4**, 1453-1458 (2017).
33. Byers, C.P. et al. Single-Particle Spectroscopy Reveals Heterogeneity in Electrochemical Tuning of the Localized Surface Plasmon. *The Journal of Physical Chemistry B* **118**, 14047-14055 (2014).
34. Willets, K.A., Wilson, A.J., Sundaresan, V. & Joshi, P.B. Super-Resolution Imaging and Plasmonics. *Chemical Reviews* **117**, 7538-7582 (2017).
35. Chen, T. et al. Optical Super-Resolution Imaging of Surface Reactions. *Chemical Reviews* **117**, 7510-7537 (2017).
36. Simoncelli, S., Li, Y., Cortés, E. & Maier, S.A. Nanoscale Control of Molecular Self-Assembly Induced by Plasmonic Hot-Electron Dynamics. *ACS Nano* **12**, 2184-2192 (2018).
37. Simoncelli, S., Li, Y., Cortés, E. & Maier, S.A. Imaging Plasmon Hybridization of Fano Resonances via Hot-Electron-Mediated Absorption Mapping. *Nano Letters* **18**, 3400-3406 (2018).
38. Jungmann, R. et al. Multiplexed 3D cellular super-resolution imaging with DNA-PAINT and Exchange-PAINT. *Nature Methods* **11**, 313 (2014).
39. Anger, P., Bharadwaj, P. & Novotny, L. Enhancement and Quenching of Single-Molecule Fluorescence. *Physical Review Letters* **96**, 113002 (2006).
40. Herne, T.M. & Tarlov, M.J. Characterization of DNA Probes Immobilized on Gold Surfaces. *Journal of the American Chemical Society* **119**, 8916-8920 (1997).
41. Zhou, X., Xu, W., Liu, G., Panda, D. & Chen, P. Size-Dependent Catalytic Activity and Dynamics of Gold Nanoparticles at the Single-Molecule Level. *Journal of the American Chemical Society* **132**, 138-146 (2010).
42. Chen, T. et al. Single-Molecule Nanocatalysis Reveals Facet-Dependent Catalytic Kinetics and Dynamics of Pallidium Nanoparticles. *ACS Catalysis* **7**, 2967-2972 (2017).
43. Chen, T., Zhang, Y. & Xu, W. Single-Molecule Nanocatalysis Reveals Catalytic Activation Energy of Single Nanocatalysts. *Journal of the American Chemical Society* **138**, 12414-12421 (2016).

44. Baffou, G., Quidant, R. & García de Abajo, F.J. Nanoscale Control of Optical Heating in Complex Plasmonic Systems. *ACS Nano* **4**, 709-716 (2010).
45. Baffou, G., Quidant, R. & Girard, C. Thermoplasmonics modeling: A Green's function approach. *Physical Review B* **82**, 165424 (2010).
46. Yoon, J.H., Selbach, F., Langolf, L. & Schlücker, S. Ideal Dimers of Gold Nanospheres for Precision Plasmonics: Synthesis and Characterization at the Single-Particle Level for Identification of Higher Order Modes. *Small* **14**, 1702754 (2018).
47. Xing, S. et al. Highly controlled core/shell structures: tunable conductive polymer shells on gold nanoparticles and nanochains. *Journal of Materials Chemistry* **19**, 3286-3291 (2009).

Table of contents entry (TOC)

Nanoscopic inspection of reactivity in single plasmonic photocatalysts.